iScience

CellPress

Article

Ternary Heterostructural Pt/CN_x/Ni as a Supercatalyst for Oxygen Reduction

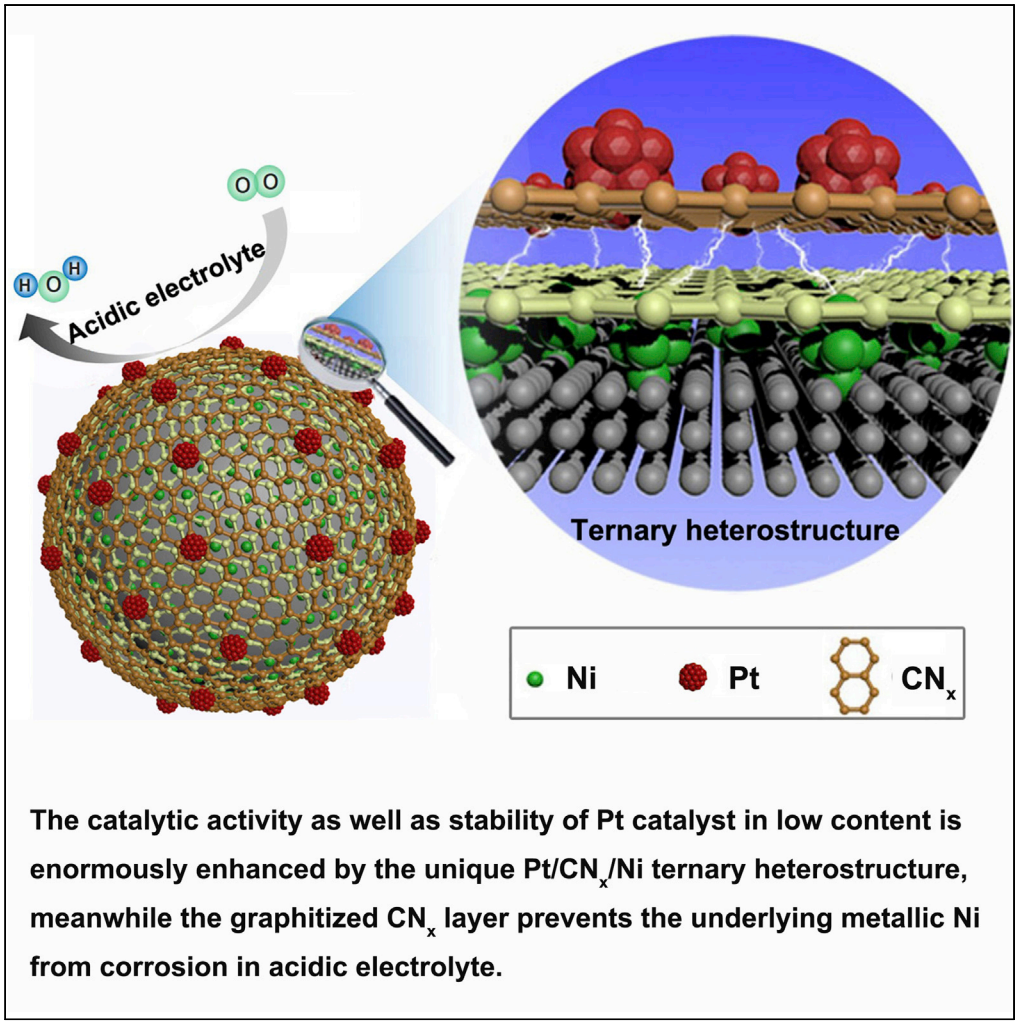

The catalytic activity as well as stability of Pt catalyst in low content is enormously enhanced by the unique Pt/CN_x/Ni ternary heterostructure, meanwhile the graphitized CN_x layer prevents the underlying metallic Ni from corrosion in acidic electrolyte.

Teng Chen, Yida Xu, Siqi Guo, ..., Zhaoxu Chen, Bin Zhao, Weiping Ding

binzhao@nju.edu.cn (B.Z.)
dingwp@nju.edu.cn (W.D.)

HIGHLIGHTS

Matched band structures among Pt/CN_x/Ni enable electron transfer from Ni to Pt

Enhanced Pt-CN_x interaction by underlying Ni prevents Pt from coalescence and oxidation

Encapsulated Ni is protected from corrosion and maintains the structure stability of THS

Chen et al., iScience *11*, 388–397
January 25, 2019
https://doi.org/10.1016/j.isci.2018.12.029

iScience

CellPress

Article

Ternary Heterostructural Pt/CN_x/Ni as a Supercatalyst for Oxygen Reduction

Teng Chen,[1] Yida Xu,[1] Siqi Guo,[1] Dali Wei,[1] Luming Peng,[1] Xuefeng Guo,[1] Nianhua Xue,[1] Yan Zhu,[1] Zhaoxu Chen,[1] Bin Zhao,[1,*] and Weiping Ding[1,2,*]

SUMMARY

We report here a supercatalyst for oxygen reduction of Pt/CN_x/Ni in a unique ternary heterostructure, in which the Pt and the underlying Ni nanoparticles are separated by two to three layers of nitrogen-doped carbon (CN_x), which mediates the transfer of electrons from the inner Ni to the outer Pt and protects the Ni against corrosion at the same time. The well-engineered low-Pt catalyst shows ~780% enhanced specific mass activity or 490% enhanced specific surface activity compared with a commercial Pt/C catalyst toward oxygen reduction. More importantly, the exceptionally strong tune on the Pt by the unique structure makes the catalyst superbly stable, and its mass activity of 0.72 A/mg_{Pt} at 0.90 V (well above the US Department of Energy's 2020 target of 0.44 A/mg_{Pt} at 0.90 V) after 50,000 cyclic voltammetry cycles under acidic conditions is still better than that of the fresh commercial catalyst.

INTRODUCTION

As a clean energy conversion device, the proton exchange membrane fuel cell (PEMFC) will shoulder the main responsibility together with secondary battery in the coming renewable energy era (Stephens et al., 2016; He et al., 2018; Zhang et al., 2018a, 2018b; Dong et al., 2018; Mo et al., 2018). However, the high amount of Pt used in the cathode catalyst for oxygen reduction reaction (ORR) is the most serious obstacle for its practical application (Wang et al., 2015; Peng and Yang, 2009). At present, the amount of Pt used in the cathode catalyst of PEMFC is commonly about 0.1–0.5 mg cm^{-2}, approximately an order of magnitude higher than that of the target set by the US Department of Energy (DOE, <0.03 mg•cm^{-2}) (Debe, 2012; Zhou et al., 2010). Although great progresses about the designs of low-Pt catalysts have been made continuously (Chen et al., 2007, 2014; Zhang et al., 2015; Wang et al., 2016; Tao et al., 2018), the high-performance ORR catalysts facilely prepared and simultaneously satisfying the demands of low Pt content, high activity, and high stability have been scarcely reported and restricted the commercial applications of PEMFC.

The well-known method to decrease Pt loading by alloying the Pt with one of transition metals (TMs) to form Pt-skin or core-shell bimetallic nanoalloys has been extensively explored, and such catalysts with relatively lower Pt contents often show much enhanced ORR activity due to the downshift of the d-band center of Pt modulated by the inner TMs through electronic effect or strain effect (Lai et al., 2018; Greeley et al., 2009; Hoster et al., 2010; Stamenkovic et al., 2006; Jiang et al., 2017; Du et al., 2015; Li et al., 2018a, 2018b). Unfortunately, the devastation of the designed alloys under real operation conditions (corrosive, oxidizing atmosphere, and high potential, >1.5 V under frequent start-up/shut-down operations) (Zhang et al., 2018a, 2018b; Gasteiger et al., 2005; Banham et al., 2015), leading to the preferred leaching of TMs (the smaller the particle, the faster the leaching), almost surely and rapidly weakens or eliminates the aforementioned modulation (Cui et al., 2012, 2013; Chi et al., 2015). Therefore most of the alloy catalysts failed to meet the DOE 2020 targets on Pt activity and durability (0.44 A/mg_{Pt} for membrane electrode assembly (MEA) in mass activity and <40% loss in mass activity after 30,000 cycles) (Li et al., 2018a, 2018b). In addition, the nanoparticles (NPs) of metallic alloys are commonly prepared using oleic acid or oleylamine as coordinating and capping ligands, which leads to technical difficulty in the following surface cleaning (Liu et al., 2018a, 2018b; Jiang et al., 2017; Li and Wong, 2018).

We report here a supercatalyst that meets well the abovementioned criteria with a unique ternary structure of Pt/CN_x/Ni, in which the Pt and the underlying Ni NPs are separated by two to three layers of nitrogen-doped carbon (CN_x), which mediate the transfer of electrons from the inner Ni to the outer Pt and protect the Ni against corrosion at the same time. The well-engineered ternary heterostructure (THS) Pt/CN_x/Ni catalyst possesses the following merits: (1) the matched band structures among the Pt, CN_x, and Ni enable

[1]Key Laboratory of Mesoscopic Chemistry, School of Chemistry and Chemical Engineering, Nanjing University, Nanjing 210093, China

[2]Lead Contact

*Correspondence: binzhao@nju.edu.cn (B.Z.), dingwp@nju.edu.cn (W.D.)

https://doi.org/10.1016/j.isci.2018.12.029

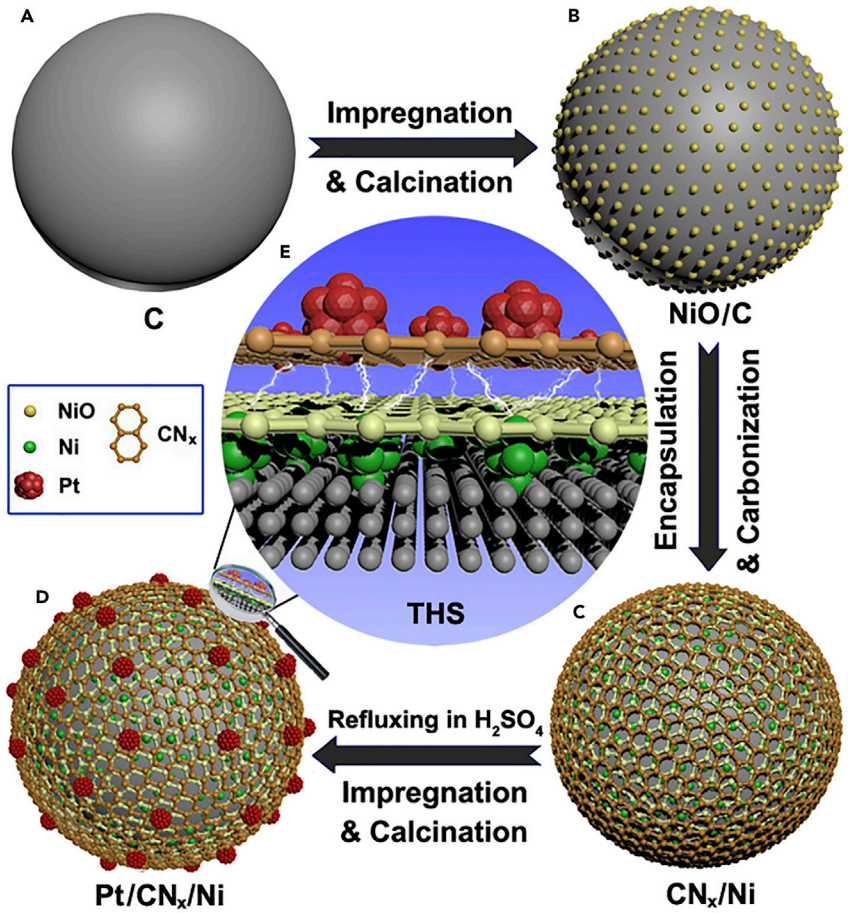

Figure 1. Schematic Illustration of the Pt/CN_x/Ni Catalyst

(A) Original carbon support (C, Vulcan XC-72R).

(B) Loading NiO NPs onto the carbon support through impregnation and calcination.

(C) Encapsulating the NiO/C with CN_x layers and the reduction of NiO NPs to metallic Ni in the meantime.

(D) Depositing Pt NPs on CN_x/Ni through impregnation and reduction.

(E) Enlarged THS: the electronic properties of the outer Pt NPs are modulated by the penetrated electrons from the inner Ni NPs through CN_x layers; meanwhile the inner Ni NPs are protected by CN_x layers from corrosion and oxidation.

electrons to transfer from the inner Ni to the outer Pt and significantly promote the ORR activity of the low-Pt catalyst; (2) the graphitized CN_x layer prevents the underlying Ni NPs from corrosion and maintains the designed structure enduringly; (3) the strengthened interaction between the Pt NPs and the electron-enriched CN_x/Ni support mitigates the agglomeration or detachment of Pt NPs significantly during the electrochemical process; and (4) the Pt NPs are protected from oxidation by the electron-enriched microenvironment, just like the strategy of "cathodic protection with sacrificial anode" in the corrosion prevention system (Abootalebi et al., 2010). Besides, the facile synthetic procedure of the THS Pt/CN_x/Ni catalyst is suitable for its scalable manufacture. We think that the novelty of current work makes a solid progress of the low-Pt catalyst for PEMFC toward practical applications.

RESULTS

Synthesis and Characterizations of CN_x/Ni and Pt/CN_x/Ni

As illustrated in Figure 1, NiO/C was first prepared by loading NiO on a nanocarbon support in globular shape and then encapsulated with the precursor of CN_x. After calcination in inert atmosphere, the CN_x/Ni/C (denoted as CN_x/Ni for clarity) support was obtained. The Pt/CN_x/Ni catalyst was prepared by depositing and reducing Pt NPs on the CN_x/Ni, which was fully rinsed in acid solution before the deposition (see Transparent Methods). The disappearance of the characteristic peaks of NiO in X-ray diffraction

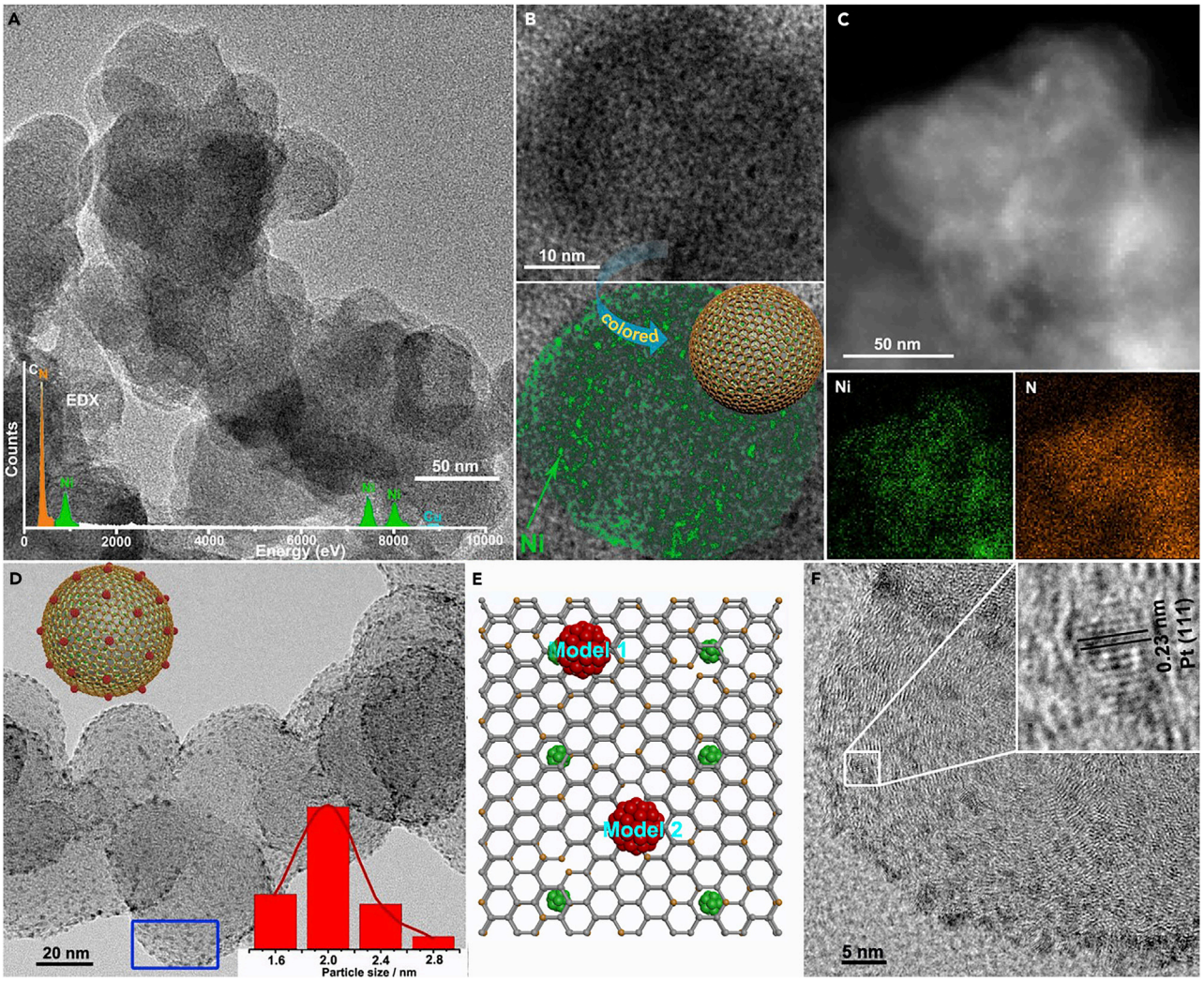

Figure 2. Morphology and Composition Characterization of the CN_x/Ni and Pt/CN_x/Ni

(A) Representative TEM image of CN_x/Ni. The CN_x/Ni are spherical with a diameter of ~30 nm. Inset: the EDX spectrum of CN_x/Ni.

(B) HRTEM image of CN_x/Ni. To reveal the distribution of Ni nanoparticles clearly, a colored image of Ni and a cartoon picture of CN_x/Ni are shown below the HRTEM image.

(C) Dark-field HAADF-STEM image of CN_x/Ni and its corresponding elemental mappings of Ni and N. These dense but uniform bright spots confirm the homogeneous distribution of Ni NPs.

(D) TEM image of the Pt/CN_x/Ni. The top left inset shows its cartoon picture, and the lower right inset is the size distribution histogram in the range of 1.6–2.8 nm by statistical analysis of 300 Pt NPs.

(E) The relative positions of Pt and Ni in Pt/CN_x/Ni sample: deduced from the structural model of the catalyst. (1) The Pt lies just above the Ni and (2) the Pt lies above but at the mid-position of the two Ni.

(F) HRTEM images of Pt/CN_x/Ni. The primary lattice spacing is ~0.23 nm, consistent with the (111) interplanar distance of cubic Pt.

(XRD) pattern and the strong magnetism of CN_x/Ni (see Figure S1) reveals that the NiO NPs are reduced to the metallic state after encapsulating with precursor of CN_x layer and calcination in N_2. Note that the strong magnetism of CN_x/Ni was retained after rinsing in acid solution, suggesting that the Ni NPs were encapsulated in and protected by the CN_x shell. The transmission electron microscopic (TEM) image of CN_x/Ni (Figure 2A) shows that the powders of CN_x/Ni are spherical with a diameter of ~30 nm. The strong characteristic peaks detected by TEM energy-dispersive X-ray spectroscopy (inset in Figure 2A) confirm the coexistence of Ni, C, and N elements. The atomic ratio of C/N is about 11, indicating that the CN_x matrix is a nitrogen-doped carbon material. The high-resolution TEM (HRTEM) image depicted in Figure 2B reveals that the Ni NPs are distributed densely and uniformly beneath the CN_x layers at an average size of about 1 nm. To reveal the distribution of Ni NPs clearly, a colored image of Ni in CN_x/Ni is shown below

the HRTEM image (Figure 2B, lower), and the dark-field High-angle annular dark field-scanning transmission electron microscopy (HAADF-STEM) image of CN_x/Ni with the dense and uniform bright spots shown in Figure 2C further confirms the homogeneous distribution of Ni NPs. Furthermore, the energy dispersive X-ray (EDX) elemental mappings of Ni and N below the STEM image (Figure 2C, lowers) reconfirm their uniformly distributed state.

Because of the similar image characteristics of carbon support and CN_x shell, the image information of CN_x is difficult to detect in CN_x/Ni. A control sample with the CN_x layers coated on nano-Al_2O_3 was prepared using the same method. As shown in Figure S2, the Al_2O_3 nanorods are ideally encapsulated in CN_x shell with a thickness of ~1.5 nm. The ~16 wt % weight loss measured by thermogravimetry during heating in air to 1,173 K (see Figure S3) indicates that the thickness of CN_x is approximately two to three layers, considering the surface area of precursor NiO/C (116.3 m^2/g, see Figure S4 and Equation S1). The results are also coincident with the change of Ni content in the samples before and after CN_x coating.

Using the CN_x/Ni as support, the THS catalyst of Pt/CN_x/Ni (for clarity, the core globular C is omitted) was prepared by impregnating chloroplatinic acid to the support, which was treated by polydopamine before the impregnation to make its surface hydrophobic and to help the dispersion of Pt (Kitagawa and Uemura, 2005; Han et al., 2018; Lee et al., 2007). As shown in Figure 2D, after heat treatment in 5.05 vol % H_2/N_2 at 673 K, the Pt NPs distribute on the spherical surface of CN_x layer evenly in the size range of 1.6–2.8 nm. It should be pointed out that the consistency between the XRD characteristic peaks of Pt in the sample and the standard JCPDS (No. 04-0850) card (see Figure S1) provides evidence to object the formation of Ni-Pt alloy (Cui et al., 2012), indicative of the separation of Ni and Pt NPs by the CN_x layer according to the THS, which is further confirmed by the subsequent electrochemical tests. The contents of Ni and Pt in Pt/CN_x/Ni measured by X-ray fluorescence (XRF) analyzer are 5.6 and 6.2 wt %, and the same measured by inductively coupled plasma mass spectrometry (ICP-MS) analysis are 5.3 and 6.6 wt %, respectively, which are consistent with each other. Based on these data, i.e., the contents and sizes of Ni and Pt, the surface area of the core nanocarbon and the CN_x/Ni (see Figure S5), and the average thickness of the CN_x, the distances between the adjacent NPs of Ni and Pt are calculated in the range of 1.5–2.5 nm (see Equation S2), as shown in Figures 1 and 2E. The HRTEM image (Figure 2F) displays the metal NP on the spherical CN_x/Ni supports a primary lattice spacing of 0.23 nm, consistent with the (111) interplanar distance of cubic Pt, excluding the formation of Pt-Ni alloy.

X-Ray Photoelectron Spectroscopy

In previous work, we have demonstrated the charge transfer at the interface of CN_x/Ni heterojunction because of the different Fermi levels of Ni and CN_x matrix (Fu et al., 2014; Chen et al., 2017). The CN_x layer is electron-rich after accepting electrons donated from Ni (see Figure S6). When Pt NPs are deposited on such an electron-rich CN_x layer, modulation on the electronic property of Pt is also detected. The binding energies of N1s in Pt/CN_x/Ni shift positively with respect to those of CN_x/Ni (Figure 3A) and there is a clear shift of $4f_{7/2}$ and $4f_{5/2}$ peaks by ~ 0.4 eV to lower binding energies for Pt/CN_x/Ni with respect to that in commercial Pt/C (20%, Alfa), suggesting the charge transfer from CN_x matrix to Pt at the interface of Pt/CN heterojunction (Liu et al., 2018a, 2018b). The electron-deficient state, to some extent, of metallic nickel in CN_x/Ni (Figure 3C) is determined by Ni binding energy due to charge transfer from the Ni to CN_x matrix (Zhao et al., 2008; Zhu et al., 2018; Fang et al., 2018; Lv et al., 2018), and interestingly, the Ni $2p_{3/2}$ peak in Pt/CN_x/Ni further increases to a higher binding energy compared with CN_x/Ni. This shift suggests that the original equilibrium of Fermi levels between Ni and CN_x layer is thrown off with the addition of Pt NPs, and a new one is established among Ni, CN_x matrix and Pt in the THS structure (Pt/CN_x/Ni). Combined with the binding energy shifts of N1s and Pt 4f, we deduce that the metallic Ni, mediated by the CN_x, can increase the electron density of Pt NPs. The surface composition of the catalyst is found as 73.5, 6.4, 8.1, 5.2, and 6.8 wt % for C, N, O, Ni, and Pt, respectively, which seem reasonable when compared with the results of XRF and ICP-MS analysis.

Theoretical Calculations

To verify the feasibility of the electron transfer, the density of states (DOS) of the elements were calculated based on the density functional theory and are shown in Figure 4. The higher Fermi level of Ni (−0.63 eV) relative to those of pyridinic N (−3.6 eV), pyrrolic N (−4.1 eV), and graphitic N (−2.0 eV) and the positive integrations for pyridinic N (0.45), pyrrolic N (0.20), and graphitic N (0.12) by integrating the DOS between Fermi levels of Ni and each nitrogen species suggest that Ni can donate its electrons to the CN_x matrix. The Fermi levels of each nitrogen species would shift positively along with the increased electron density due to

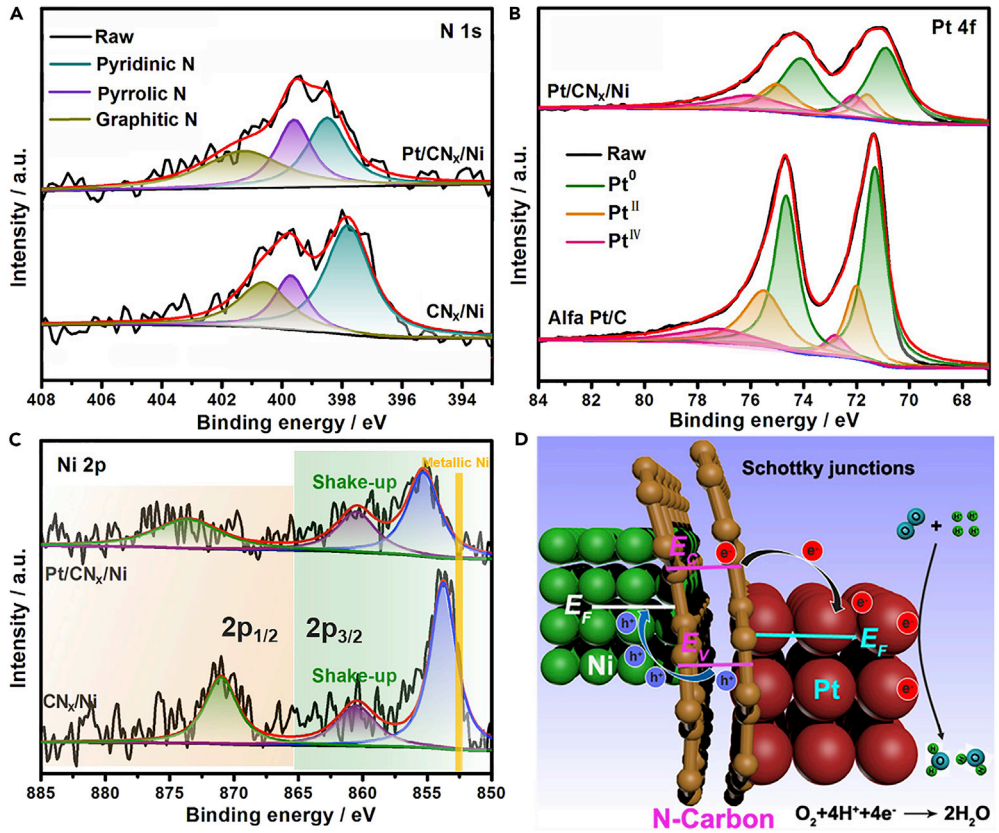

Figure 3. Electronic Equilibration across the CN_x/Ni and Pt/CN_x Interfaces and the Results of XPS

(A–C) Deconvoluted spectra of nitrogen 1s (A), platinum 4f (B), and nickel 2p (C) in CN/Ni and Pt/CN_x/Ni.

(D) Schematic illustration for Mott-Schottky-type contacts of Pt/CN_x/Ni in the THS structure.

The negative shifts of Pt_{4f} binding energies and the more positive shifts of Ni_{2p} binding energies in Pt/CN_x/Ni indicating the charge transfer from Ni to Pt through CN_x.

the electron transfer at the interface of the CN_x/Ni heterojunction (Subramanian et al., 2004). In addition, the relatively lower Fermi level of Pt (−4.22 eV) also enables it to accept electrons from the CN_x matrix easily. Such charge transfer is also corroborated by the shift of conduction band in samples with or without Ni or Pt (Figure S7).

Based on the discussion above, an illustration for Mott-Schottky-type contacts in Pt/CN_x/Ni THS is shown in Figure 3D. Owing to the different Fermi levels among the CN_x matrix and metallic Ni and Pt, the charges will transfer spontaneously from Ni to Pt, mediated by the CN_x, until their Fermi levels reach equilibrium (Deng et al., 2016). The charge transfer will surely affect the electronic properties, and thus the adsorption/desorption properties of the Pt NPs for oxygen species on their surfaces. Redox of O_2-H_2 titration profiles in Figure S8 supports this viewpoint. The lower onset of reduction temperature of chemisorbed oxygen on Pt/CN_x/Ni (~300°C) than that of Pt/C (~400°C) suggests the higher reactivity of the oxygen species adsorbed on Pt/CN_x/Ni catalyst, which is beneficial to enhance its ORR catalytic activity. The results of the CO stripping measurement (Figure S9) show that the main peaks of CO oxidation on Pt/C, Pt/CN_x, and Pt/CN_x/Ni are located at 0.95, 0.99, and 0.85 V, respectively. Combined with the above results, it is clear that the Pt with enriched electrons can afford more active oxygen species and can lead to a lower oxidation potential (Van der Vliet et al., 2012; Igarashi et al., 2001).

Electrocatalytic Performance

To evaluate the possible relationship between the electronic structure of Pt and its catalytic activity toward ORR, the ORR polarization curves of the Pt/CN_x/Ni, Pt/CN_x, and the commercial Pt/C were measured and normalized by glassy carbon electrode geometric area (0.246 cm^2). The mass loadings of Pt on glassy

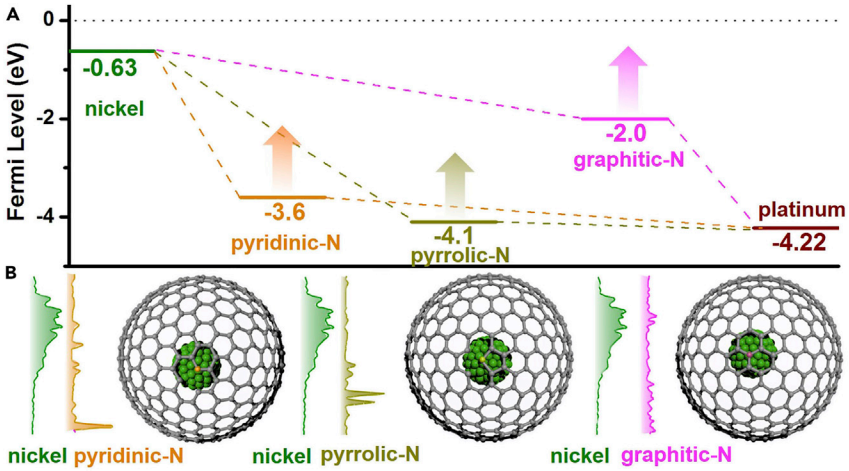

Figure 4. Electron Transfer Pathway in Pt/CN_x/Ni Heterostructures

(A) Fermi level of nickel, pyridinic-N, pyrrolic-N, graphitic-N, and platinum.

(B) The density of states (DOS) of the elements and the local structures of their interfaces. The vacuum level is aligned at 0 eV.

carbon electrode were 6.2, 6.0, and 20 μg cm^{-2}, for Pt/CN_x/Ni, Pt/CN_x, and Pt/C, respectively. As shown in Figure 5A, the half-wave potential of the sample Pt/CN_x/Ni is 0.886 V, which is higher than those of the corresponding Ni-free sample (Pt/CN_x, 0.839 V) and commercial Pt/C (0.858 V). Such positive shift of half-wave potential suggests that the presence of modulation by the underlying Ni can accelerate the separation of the adsorbed oxide species from Pt surface and thereby improve the ORR kinetics. The results of cyclic voltammetry (CV) measurements shown in Figure 5B are in favor of this interpretation. The more positive reduction potential of Pt-OH_{ad} (adsorbed hydroxyl species) in Pt/CN_x/Ni suggests that the OH_{ad} are promoted to react with H^+ to form H_2O on its electron-enriched surface (Stamenkovic et al., 2007; Wang et al., 2011).

Furthermore, the higher initiation potential of Pt oxidation features suggest that the Pt NPs are protected by the surplus electrons on its surface from oxidation, just like "cathodic protection with sacrificial anode" in corrosion prevention system (Abootalebi et al., 2010). Suppression of the formation of Pt oxide will decrease the blockage of active sites by adsorbed oxygen species and then enhance the ORR activity (Snyder et al., 2013). Different from alloy catalysts, of which the Pt electronic property is often overly tuned because of the strong electronic interaction and great lattice mismatch between Pt and parts of TMs, the rate-determining step in the volcano-type activity plots turns from desorption process (left side) to adsorption process (right side in Figure S10) (Greeley et al., 2009; Stephens et al., 2012). The overly tuned Pt catalyst with weak adsorption of oxygen also leads to an undesired decrease in catalytic activity.

To confirm that the Pt and Ni are separated in the THS, the electrochemical performance of Pt/CN_x/Ni catalyst before and after refluxing in 1 M H_2SO_4 at 353 K are measured in alkaline solution (0.1 M KOH). If the Pt and Ni are not separated by CN_x, the exposed Ni would be oxidized to NiO partially during the testing in alkaline solution and the formed NiO will dissolve in 1 M H_2SO_4 in the following refluxing process, which will influence the ORR performance. However, the coincident CV and ORR polarization curves for the samples initially and after refluxing for 3 and 6 hr, shown in Figure S11, provide further evidences of the effective protection of Ni by the CN_x shell and also to veto the formation of Ni-Pt alloy (Rudi et al., 2017). Based on the integral charge in underpotentially deposited hydrogen (H_{UPD}) adsorption/desorption region in the CV curves and the mass loading of Pt, the specific electrochemically active surface area (ECSA) of Pt/CN_x/Ni, Pt/CN_x, and Pt/C are calculated as 122.0, 125.5, and 77.2 m^2/g_{Pt}, respectively. It should be pointed out that the theoretical specific surface area of the Pt NPs in Pt/CN_x/Ni (d = 2 nm) and Pt/C (d = 3.5 nm) are 139.8 and 79.9 m^2/g_{Pt} (Equation S3), respectively, well consistent with the ECSA results. The higher specific ECSA of the Pt/CN_x/Ni catalyst is consistent with the higher H_2 consumption in O_2-H_2 titration measurements (see Figure S8).

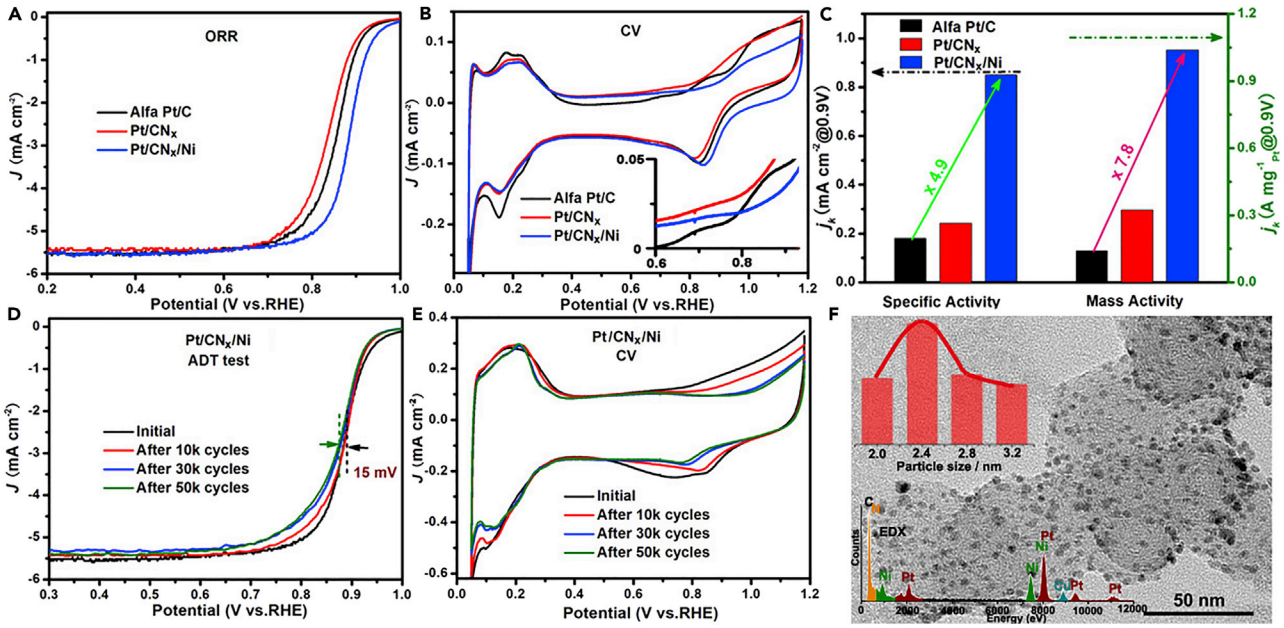

Figure 5. Electrochemical Performance of Pt/CN_x/Ni, Pt/CN_x, and Commercial Pt/C Catalysts for ORR

(A–C) (A) ORR polarization curves, (B) cyclic voltammetry (CV) curves, and (C) specific and mass activities of different catalysts at 0.9 V versus RHE.

(D and E) (D) ORR polarization curves and (E) CV curves of Pt/CN_x/Ni before and after 50,000 CV cycles between 0.6 and 1.0 V versus RHE. The scan rate for the accelerated durability test (ADT) is 200 mV s^{-1}. The curves in (A, D, and E) were recorded at 298 K in 0.1 M $HClO_4$ aqueous solution at a sweep rate of 20 mV/s, and the curves in (B) were recorded at a sweep rate of 5 mV/s.

(F) TEM image of Pt/CN_x/Ni after ADT test. Inset is the corresponding size distribution histogram and EDX spectrum.

Figure 5C shows the specific surface and specific mass activities of the samples, which are normalized by the ECSA or the mass of the loaded Pt, respectively. With 6.2 μg cm^{-2} loading of Pt, Pt/CN_x/Ni exhibits a mass activity of 1.04 A mg^{-1}_{Pt} and a specific activity of 0.85 mA cm^{-2} (at 0.9 V versus reversible hydrogen electrode (RHE)), which are 7.8 and 4.9 times higher than those of the commercial Pt/C (20 μg cm^{-2}) under the same conditions. It should be pointed out that the onset potential of CN_x/Ni support is just 0.75 V versus RHE (see Figure S12) under the same testing conditions, indicating that the catalytic contribution from support is negligible. Hence, the enhanced catalytic activity should be ascribed to the modulated electronic structure and the relatively higher specific ECSA of the Pt/CN_x/Ni catalyst. The former is the main cause, for the ECSA of Pt/CN_x/Ni is about only 1.5 times that of the Pt/C.

The catalytic stability of the Pt/CN_x/Ni catalyst was assessed by accelerated deterioration tests (ADT) at a scan rate of 200 mV s^{-1} between 0.6 and 1.0 V versus RHE in O_2-saturated 0.1 M $HClO_4$. As shown in Figure 5D, a negative shift of mere 15 mV of the half-wave potential of Pt/CN_x/Ni is observed after 50,000 sweeping cycles. However, a ~64-mV negative shift is shown for the commercial Pt/C and ~50 mV for Pt/CN_x under the same condition (Figure S13). The retention of specific ECSA for the samples are measured from H_{UPD} and listed in Table S1. After 50,000 sweeping cycles, the retention of the specific ECSA is ~90% for Pt/CN_x/Ni, much higher than that of Pt/CN_x (~73%) and Pt/C (~60%). The unique THS of Pt/CN_x/Ni mitigates the surface oxidation, detachment, and aggregation of Pt and thereby contributes to the higher ECSA retention and outstanding stability. Indeed, the designed THS of Pt/CN_x/Ni is reserved commendably after the ADT test in corrosive and oxidative environment and the TEM images of Pt/CN_x/Ni (Figure 5F) after 50,000 cycles reveal the unchanged morphology and size of the Pt NPs. In contrast, a serious aggregation of Pt NPs occurs for the commercial Pt/C, wherein the average size of Pt increases from 3.5 to 5.2 nm (Figure S14).

It should be pointed out that the THS model is also applicable to other TMs occupying suitable Fermi levels, such as cobalt. As shown in Figure S15 and Table S1, the Pt/CN_x/Co catalyst exhibits similar physical property and catalytic activity for ORR with respect to Pt/CN_x/Ni. The unique Pt/CN_x/Ni(Co) catalyst in the THS with high specific activity and superstability provides hope for practical use in fuel

cells, which simultaneously satisfies the target set by US DOE of low Pt content, high activity, and high stability.

DISCUSSION

The unique THS of Pt/CN_x/Ni catalyst has been designed and synthesized successfully using a facile and scalable method. Based on the matched band structures among the Pt, CN_x, and Ni, the electronic properties of the outer Pt NPs are properly modulated by the inner Ni, mediated by the CN_x layers, which also act as a protective shield for Ni against the corrosive and oxidative conditions. The modulation of the Pt NPs by the electron-rich CN_x/Ni support significantly promotes the activity of the catalyst, and the strong interactions between them mitigates the oxidation, detachment, and aggregation of Pt NPs under the working conditions of electrocatalysis. Benefited from the artful design of the THS, the catalyst exhibits high performance for oxygen reduction, simultaneously satisfying the target set by US DOE of low Pt content, high activity, and high stability. The catalyst will be supplied in quantity to the scientific community of fuel cells in the near future.

Limitations of Study

In the Pt/CN_x/Ni THS, the thinner the CN_x layers, the easier the electron transfer from the inner Ni to the outer Pt through CN_x layers and the higher the ORR performance of Pt catalyst. However, considering the protection of the CN_x layers for the Ni particles from corrosion, the CN_x layers should not be too thin. To study the electronic modulation of the Pt sites and the stability of Ni particles in acidic electrolyte, the influence of CN_x thickness could be explored in detail in the future.

METHODS

All methods can be found in the accompanying Transparent Methods supplemental file.

SUPPLEMENTAL INFORMATION

Supplemental Information includes Transparent Methods, 15 figures, and 1 table and can be found with this article online at https://doi.org/10.1016/j.isci.2018.12.029.

ACKNOWLEDGMENTS

The authors thank the financial supports from the Ministry of Science and Technology of China (2017YFB0702900), the National Science Foundation of China (91434101, 91745108), and Nanjing Black-Tech Co. Ltd., China.

AUTHOR CONTRIBUTIONS

W.D. conceived the work. B.Z guided the experiments. T.C. designed and performed main experiments. Y.X., S.G., and D.W. participated in the experimental work. Z.C. performed the theoretical calculations. N.X., L.P., and X.G. carried out the discussion. T.C. wrote the manuscript and B. Z. participated in the writing, and W.D. finalized the work. All authors discussed the results.

DECLARATION OF INTERESTS

The authors declare no competing interests.

Received: November 5, 2018
Revised: December 13, 2018
Accepted: December 26, 2018
Published: January 25, 2019

REFERENCES

Abootalebi, O., Kermanpur, A., Shishesaz, M., and Golozar, M. (2010). Optimizing the electrode position in sacrificial anode cathodic protection systems using boundary element method. Corros. Sci. *52*, 678–687.

Banham, D., Ye, S., Pei, K., Ozaki, J.I., Kishimoto, T., and Imashiro, Y. (2015). A review of the stability and durability of non-precious metal catalysts for the oxygen reduction reaction in proton exchange membrane fuel cells. J. Power Sources *285*, 334–348.

Chen, T., Guo, S., Yang, J., Xu, Y., Sun, J., Wei, D., Chen, Z., Zhao, B., and Ding, W. (2017). Nitrogen-doped carbon activated in situ by embedded nickel through the Mott-Schottky effect for the oxygen reduction reaction. ChemPhysChem *18*, 3454–3461.

Chen, Z., Waje, M., Li, W., and Yan, Y. (2007). Supportless Pt and PtPd nanotubes as electrocatalysts for oxygen-reduction reactions. Angew. Chem. Int. Ed. *119*, 4138–4141.

Chen, C., Kang, Y., Huo, Z., Zhu, Z., Huang, W., Xin, H.L., Snyder, J.D., Li, D., Herron, J.A., Mavrikakis, M., et al. (2014). Highly crystalline multimetallic nanoframes with three-dimensional electrocatalytic surfaces. Science *343*, 1339–1343.

Chi, M., Wang, C., Lei, Y., Wang, G., Li, D., More, K.L., Lupini, A., Allard, L.F., Markovic, N.M., and Stamenkovic, V.R. (2015). Surface faceting and elemental diffusion behaviour at atomic scale for alloy nanoparticles during in situ annealing. Nat. Commun. *6*, 8925.

Cui, C., Gan, L., Heggen, M., Rudi, S., and Strasser, P. (2013). Compositional segregation in shaped Pt alloy nanoparticles and their structural behaviour during electrocatalysis. Nat. Mater. *12*, 765–771.

Cui, C., Gan, L., Li, H.H., Yu, S.H., Heggen, M., and Strasser, P. (2012). Octahedral PtNi nanoparticle catalysts: exceptional oxygen reduction activity by tuning the alloy particle surface composition. Nano Lett. *12*, 5885–5889.

Debe, M.K. (2012). Electrocatalyst approaches and challenges for automotive fuel cells. Nature *486*, 43–50.

Deng, D., Novoselov, K.S., Fu, Q., Zheng, N., Tian, Z., and Bao, X. (2016). Catalysis with two-dimensional materials and their heterostructures. Nat. Nanotechnol. *11*, 218–230.

Dong, C., Gao, W., Jin, B., and Jiang, Q. (2018). Advances in cathode materials for high-performance lithium-sulfur batteries. iScience *6*, 151–198.

Du, M., Cui, L., Cao, Y., and Bard, A. (2015). Mechanoelectrochemical catalysis of the effect of elastic strain on a platinum nanofilm for the ORR exerted by a shape memory alloy substrate. J. Am. Chem. Soc. *137*, 7397–7403.

Fang, Z., Peng, L., Qian, Y., Zhang, X., Xie, Y., Cha, J.J., and Yu, G. (2018). Dual tuning of Ni-Co-A (A= P, Se, O) nanosheets by anion substitution and holey engineering for efficient hydrogen evolution. J. Am. Chem. Soc. *140*, 5241–5247.

Fu, T., Wang, M., Cai, W., Cui, Y., Gao, F., Peng, L., Chen, W., and Ding, W. (2014). Acid-resistant catalysis without use of noble metals: carbon nitride with underlying nickel. ACS Catal. *4*, 2536–2543.

Gasteiger, H.A., Kocha, S.S., Sompalli, B., and Wagner, F.T. (2005). Activity benchmarks and requirements for Pt, Pt-alloy, and non-Pt oxygen reduction catalysts for PEMFCs. Appl. Catal. B Environ. *56*, 9–35.

Greeley, J., Stephens, I.E.L., Bondarenko, A.S., Johansson, T.P., Hansen, H.A., Jaramillo, T.F., Rossmeisl, J., Chorkendorff, I., and Nørskov, J.K. (2009). Alloys of platinum and early transition metals as oxygen reduction electrocatalysts. Nat. Chem. *1*, 552–556.

Han, A., Chen, W., Zhang, S., Zhang, M., Han, Y., Zhang, J., Ji, S., Zhang, L., Wang, Y., Gu, L., et al. (2018). A polymer encapsulation strategy to synthesize porous nitrogen-doped carbon-nanosphere-supported metal isolated-single-atomic-site catalysts. Adv. Mater. *30*, 1706508.

He, J., Chen, Y., and Manthiram, A. (2018). MOF-derived cobalt sulfide grown on 3D graphene foam as an efficient sulfur host for long-life lithium-sulfur batteries. iScience *4*, 36–43.

Hoster, H., Alves, O., and Koper, M. (2010). Tuning adsorption via strain and vertical ligand effects. ChemPhysChem *11*, 1518–1524.

Igarashi, H., Fujino, T., Zhu, Y., Uchida, H., and Watanabe, M. (2001). CO tolerance of Pt alloy electrocatalysts for polymer electrolyte fuel cells and the detoxification mechanism. Phys. Chem. Chem. Phys. *3*, 306–314.

Jiang, K., Zhao, D., Guo, S., Zhang, X., Zhu, X., Guo, J., Lu, G., and Huang, X. (2017). Efficient oxygen reduction catalysis by subnanometer Pt alloy nanowires. Sci. Adv. *3*, e1601705.

Kitagawa, S., and Uemura, K. (2005). Dynamic porous properties of coordination polymers inspired by hydrogen bonds. Chem. Soc. Rev. *34*, 109–119.

Lai, J., Huang, B., Tang, Y., Lin, F., Zhou, P., Chen, X., Sun, Y., Lv, F., and Guo, S. (2018). Barrier-free interface electron transfer on PtFe-Fe_2C janus-like nanoparticles boosts oxygen catalysis. Chem *4*, 1153–1166.

Lee, H., Dellatore, S., Miller, W., and Messersmith, P. (2007). Mussel-inspired surface chemistry for multifunctional coatings. Science *318*, 426–430.

Li, J., Xi, Z., Pan, Y.T., Spendelow, J.S., Duchesne, P.N., Su, D., Li, Q., Yu, C., Yin, Z., Shen, B., et al. (2018a). Fe stabilization by intermetallic $L1_0$-FePt and Pt catalysis enhancement in $L1_0$-FePt/Pt nanoparticles for efficient oxygen reduction reaction in fuel cells. J. Am. Chem. Soc. *140*, 2926–2932.

Li, J., Sharma, S., Liu, X., Pan, Y.T., Spendelow, J.S., Chi, M., Jia, Y., Zhang, P., Cullen, D.A., Xi, Z., et al. (2018b). Hard-magnet L10-CoPt nanoparticles advance fuel cell catalysis. Joule *3*, 1–12.

Li, L., and Wong, S.S. (2018). Ultrathin metallic nanowire-based architectures as high-performing electrocatalysts. ACS Omega *3*, 3294–3313.

Liu, L., Liu, Y., Ai, Y., Li, J., Zhou, J., Fan, Z., Bao, H., Jiang, R., Hu, Z., Wang, J., et al. (2018a). Pd-CuFe catalyst for transfer hydrogenation of Nitriles: controllable selectivity to primary amines and secondary amines. iScience *8*, 61–73.

Liu, Z., Qi, J., Liu, M., Zhang, S., Fan, Q., Liu, H., Liu, K., Zheng, H., Yin, Y., and Gao, C. (2018b). Aqueous synthesis of ultrathin platinum/non-noble metal alloy nanowires for enhanced hydrogen evolution activity. Angew. Chem. Int. Ed. *130*, 11852–11856.

Lv, C., Qian, Y., Yan, C., Ding, Y., Liu, Y., Chen, G., and Yu, G. (2018). Defect engineering metal-free polymeric carbon nitride electrocatalyst for effective nitrogen fixation under ambient conditions. Angew. Chem. Int. Ed. *57*, 10246–10250.

Mo, R., Rooney, D., and Sun, K. (2018). Uniform yolk-shell germanium@ polypyrrole architecture with precision expansion void control for high-performance lithium ion batteries. iScience *9*, 521–531.

Peng, Z., and Yang, H. (2009). Designer platinum nanoparticles: control of shape, composition in alloy, nanostructure and electrocatalytic property. Nano Today *4*, 143–164.

Rudi, S., Teschner, D., Beermann, V., Hetaba, W., Gan, L., Cui, C., Gliech, M., Schlögl, R., and Strasser, P. (2017). pH-induced versus oxygen-induced surface enrichment and segregation effects in Pt-Ni alloy nanoparticle fuel cell catalysts. ACS Catal. *7*, 6376–6384.

Snyder, J., Livi, K., and Erlebacher, J. (2013). Oxygen reduction reaction performance of [MTBD][beti]-encapsulated nanoporous NiPt alloy nanoparticles. Adv. Funct. Mater. *23*, 5494–5501.

Stamenkovic, V., Mun, B.S., Mayrhofer, K.J., Ross, P.N., Markovic, N.M., Rossmeisl, J., Greeley, J., and Nørskov, J.K. (2006). Changing the activity of electrocatalysts for oxygen reduction by tuning the surface electronic structure. Angew. Chem. Int. Ed. *118*, 2963–2967.

Stamenkovic, V.R., Fowler, B., Mun, B.S., Wang, G., Ross, P.N., Lucas, C.A., and Marković, N.M. (2007). Improved oxygen reduction activity on Pt_3Ni (111) via increased surface site availability. Science *315*, 493–497.

Stephens, I.E.L., Rossmeisl, J., and Chorkendorff, I. (2016). Toward sustainable fuel cells. Science *354*, 1378–1379.

Stephens, I., Bondarenko, A., Grønbjerg, U., Rossmeisl, J., and Chorkendorff, I. (2012). Understanding the electrocatalysis of oxygen reduction on platinum and its alloys. Energy Environ. Sci. *5*, 6744–6762.

Subramanian, V., Wolf, E.E., and Kamat, P.V. (2004). Catalysis with TiO_2/gold nanocomposites. Effect of metal particle size on the Fermi level equilibration. J. Am. Chem. Soc. *126*, 4943–4950.

Tao, L., Yu, D., Zhou, J., Lu, X., Yang, Y., and Gao, F. (2018). Ultrathin wall (1 nm) and superlong Pt nanotubes with enhanced oxygen reduction reaction performance. Small *14*, 1704503.

Van der Vliet, D., Wang, C., Li, D., Paulikas, A.P., Greeley, J., Rankin, R.B., Strmcnik, D., Tripkovic, D., Markovic, N.M., and Stamenkovic, V.R. (2012). Unique electrochemical adsorption properties of Pt-skin surfaces. Angew. Chem. Int. Ed. *124*, 3193–3196.

Wang, X., Figueroa-Cosme, L., Yang, X., Luo, M., Liu, J., Xie, Z., and Xia, Y. (2016). Pt-based icosahedral nanocages: using a combination of {111} facets, twin defects, and ultrathin walls to greatly enhance their activity toward oxygen reduction. Nano Lett. *16*, 1467–1471.

Wang, Y.J., Zhao, N., Fang, B., Li, H., Bi, X.T., and Wang, H. (2015). Carbon-supported Pt-based alloy electrocatalysts for the oxygen reduction reaction in polymer electrolyte membrane fuel cells: particle size, shape, and composition manipulation and their impact to activity. Chem. Rev. *115*, 3433–3467.

Wang, C., Chi, M., Li, D., Strmcnik, D., van der Vliet, D., Wang, G., Komanicky, V., Chang, K.C., Paulikas, A.P., Tripkovic, D., et al. (2011). Design and synthesis of bimetallic electrocatalyst with multilayered Pt-skin surfaces. J. Am. Chem. Soc. *133*, 14396–14403.

Zhang, L., Roling, L.T., Wang, X., Vara, M., Chi, M., Liu, J., Choi, S., Park, J., Herron, J.A., Xie, Z., et al. (2015). Platinum-based nanocages with subnanometer-thick walls and well-defined, controllable facets. Science *349*, 412–416.

Zhang, G.R., Wolker, T., Sandbeck, D.J., Munoz, M., Mayrhofer, K.J., Cherevko, S., and Etzold, B.J. (2018a). Tuning the electrocatalytic performance of ionic liquid modified Pt catalysts for the oxygen reduction reaction via cationic chain engineering. ACS Catal. *8*, 8244–8254.

Zhang, W., Zu, L., Kong, B., Chen, B., He, H., Lan, K., Liu, Y., Yang, J., and Zhao, D. (2018b). Mesoporous TiO_2/TiC@ C composite membranes with stable TiO_2-C interface for robust lithium storage. iScience *3*, 149–160.

Zhao, Z., Wu, Z., Zhou, L., Zhang, M., Li, W., and Tao, K. (2008). Synthesis of a nano-nickel catalyst modified by ruthenium for hydrogenation and hydrodechlorination. Catal. Commun. *9*, 2191–2194.

Zhou, Y., Neyerlin, K., Olson, T., Pylypenko, S., Bult, J., Dinh, H., Gennett, T., Shao, Z., and O'Hayre, R. (2010). Enhancement of Pt and Pt-alloy fuel cell catalyst activity and durability via nitrogen-modified carbon supports. Energy Environ. Sci. *3*, 1437–1446.

Zhu, Y., Peng, L., Fang, Z., Yan, C., Zhang, X., and Yu, G. (2018). Structural engineering of 2D nanomaterials for energy storage and catalysis. Adv. Mater. *30*, 1706347.

ISCI, Volume *11*

Supplemental Information

Ternary Heterostructural Pt/CN_x/Ni as a Supercatalyst for Oxygen Reduction

Teng Chen, Yida Xu, Siqi Guo, Dali Wei, Luming Peng, Xuefeng Guo, Nianhua Xue, Yan Zhu, Zhaoxu Chen, Bin Zhao, and Weiping Ding

Supplemental Information

Supplemental Data Items

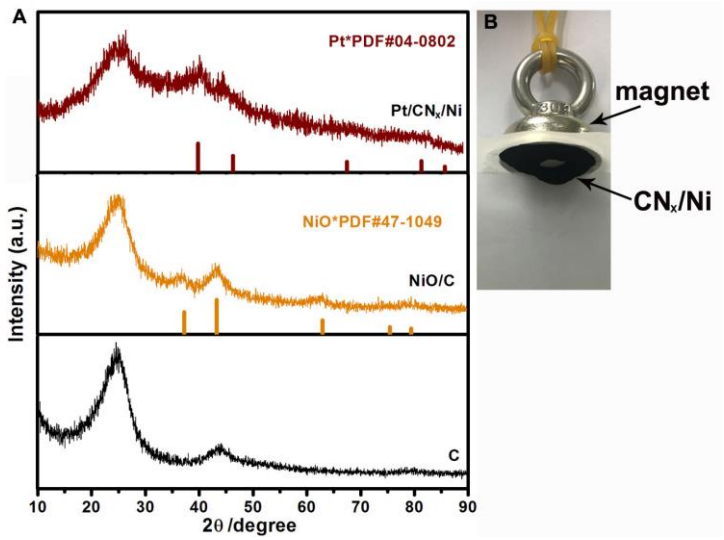

Figure S1. Characterization of as-prepared $Pt/CN_x/Ni$ and the intermediates in its preparation process, related to Figure 2. (A) XRD patterns for $Pt/CN_x/Ni$ and the intermediates in its preparation process, (B) a picture of adsorbed CN_x/Ni on magnet to reveal the magnetism of CN_x/Ni.

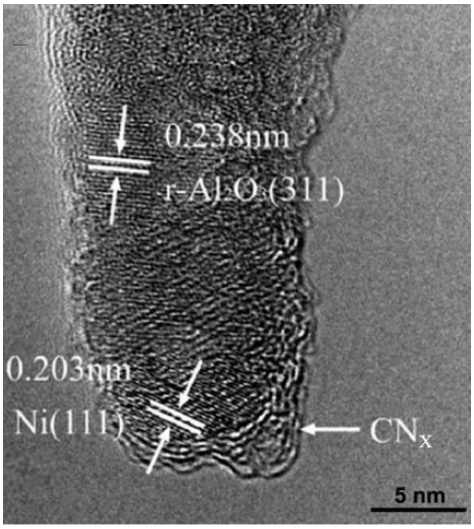

Figure S2. Characterization of $CN_x/Ni/Al_2O_3$, related to Figure 2. HRTEM images of $CN_x/Ni/Al_2O_3$. The thickness of CN_x is approximately 1.5 nm.

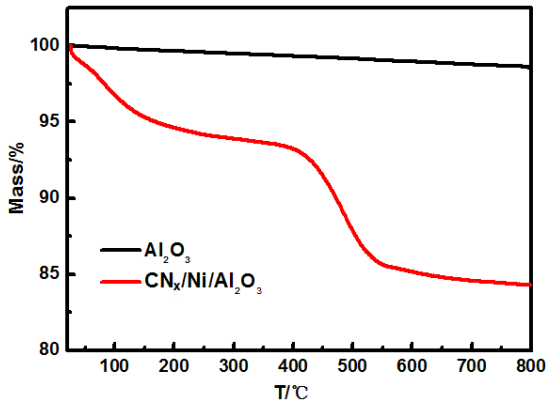

Figure S3. Characterization of Al_2O_3 and $CN_x/Ni/Al_2O_3$, related to Figure 2. Thermogravimetric profiles for Al_2O_3 and $CN_x/Ni/Al_2O_3$.

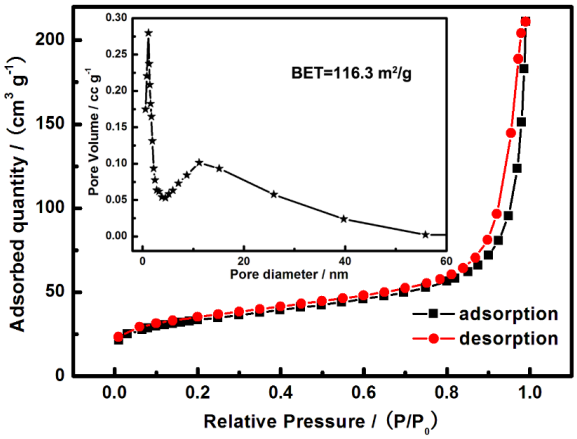

Figure S4. Characterization of NiO/C, related to Figure 2. N_2 adsorption/desorption isotherms and pore size distributions of NiO/C.

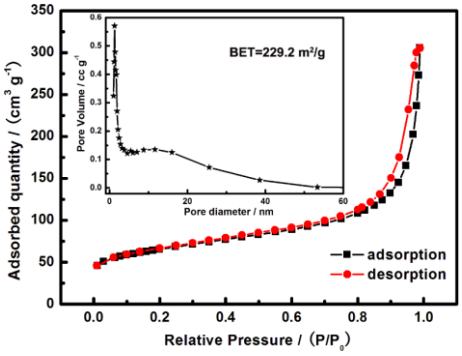

Figure S5. Characterization of XC-72R support, related to Figure 2. N_2 adsorption/desorption isotherms and pore size distributions of C.

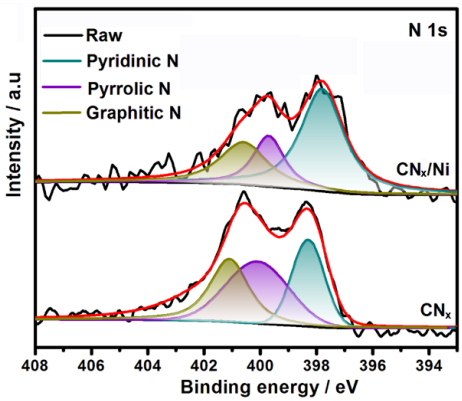

Figure S6. Electronic equilibration across the CN_x/Ni interface, related to Figure 3. Deconvoluted spectra of nitrogen 1s of CN_x/Ni and CN_x.

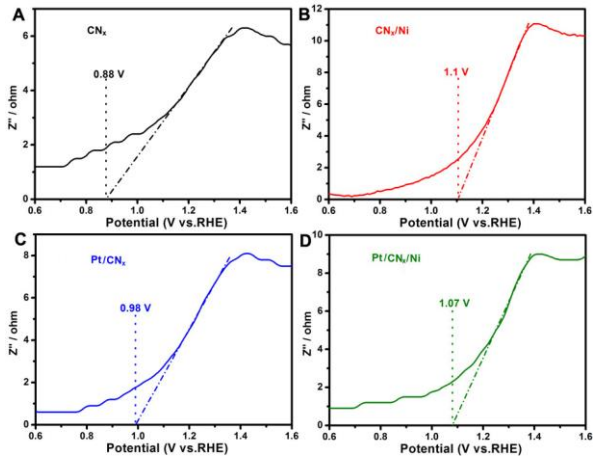

Figure S7. The electrochemical study of CN_x, CN_x/Ni, Pt/CN_x and Pt/CN_x/Ni, related to Figure 3. Impedance-potential curves of (A) CN_x, (B) CN_x/Ni, (C) Pt/CN_x and (D) Pt/CN_x/Ni for determining the flat-band potentials of samples.

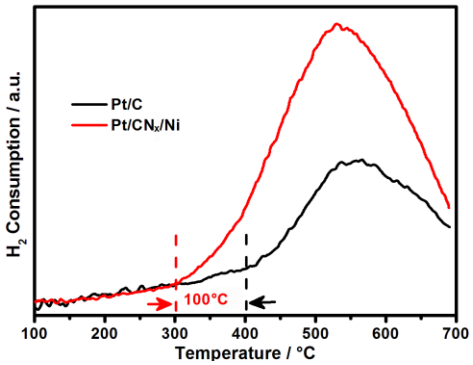

Figure S8. Characterization of Pt/C and Pt/CN_x/Ni, related to Figure 5. Redox O_2-H_2 titration curves for Pt/C and Pt/CN_x/Ni.

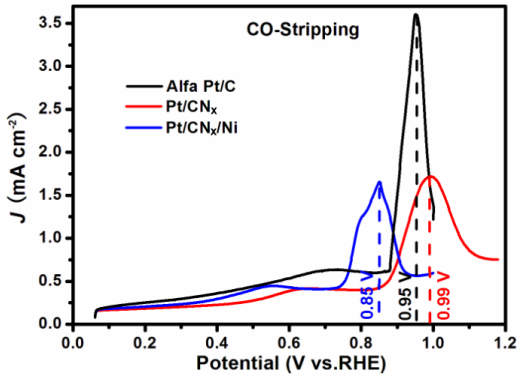

Figure S9. The electrochemical study of Pt/C, Pt/CN$_x$ and Pt/CN$_x$/Ni, related to Figure 5.
CO-Stripping curves of Alfa Pt/C, Pt/CN$_x$ and Pt/CN$_x$/Ni for probing the adsorption properties of the Pt catalysts.

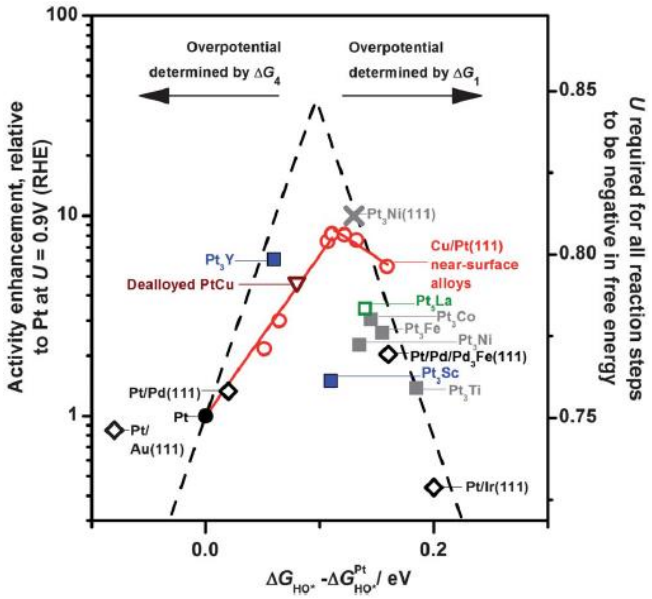

Figure S10. The rate-determining step in the volcano type activity plots, related to Figure 5. Volcano plot for different catalysts with Pt-overlayers: experimental ORR activity enhancement as a function of hydroxyl binding energy, ΔG_{HO}*, both relative to pure Pt. All data are at U = 0.9 V, with respect to a reversible hydrogen electrode (RHE) (Stephens et al., 2012).

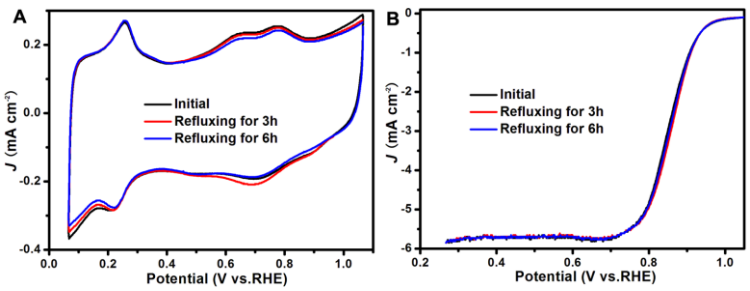

Figure S11. The electrochemical study of Pt/CN$_x$/Ni electrode, related to Figure 5. (A), CV curves and (B), ORR polarization curves of Pt/CN$_x$/Ni catalyst before and after refluxing in 1 M H_2SO_4 at 353 K in alkaline solution (0.1 M KOH). The scan rate is 20 mV s^{-1}.

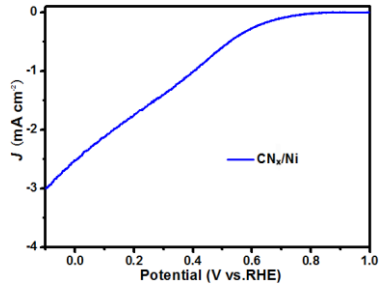

Figure S12. The electrochemical study of Pt/CN_x/Ni electrode, related to Figure 5. ORR polarization curves of CN_x/Ni in 0.1M $HClO_4$ aqueous solution at a sweep rate of 20 mV s^{-1}.

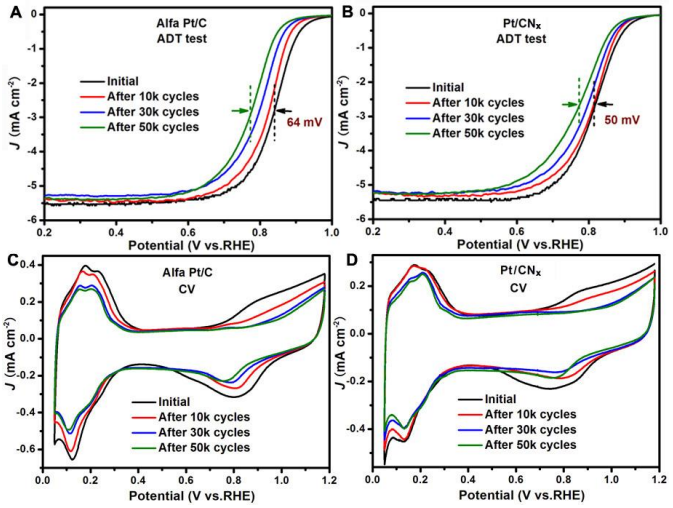

Figure S13. The stability study of Pt/C and Pt/CN_x electrodes, related to Figure 5. ORR polarization curves of Alfa Pt/C (A) and Pt/CN_x (B), CV curves of Alfa Pt/C (C) and Pt/CN_x (D) before and after 50000 CV cycles between 0.6 and 1.0 V versus RHE. The sweep rate for the accelerated deterioration test (ADT) is 200 mV s^{-1}. All the curves were recorded at 298 K in 0.1M $HClO_4$ aqueous solution at a sweep rate of 20 mV s^{-1}.

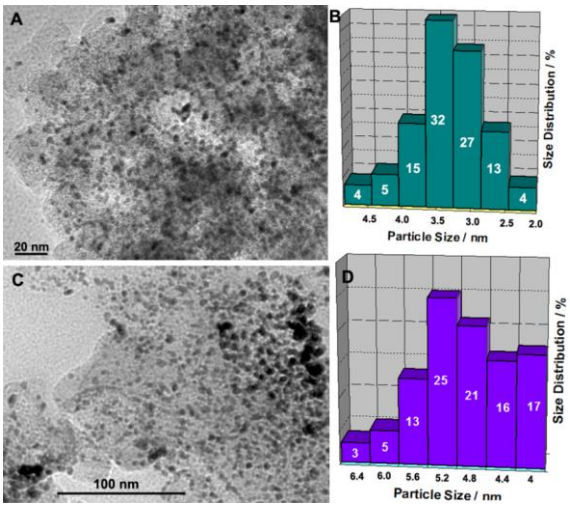

Figure S14. Characterization of Pt/C, related to Figure 5. TEM images of commercial Pt/C (Alfa) before (A) and after (C) ADT test, and their corresponding size distribution histogram by statistical analysis of 300 Pt NPs (B and D).

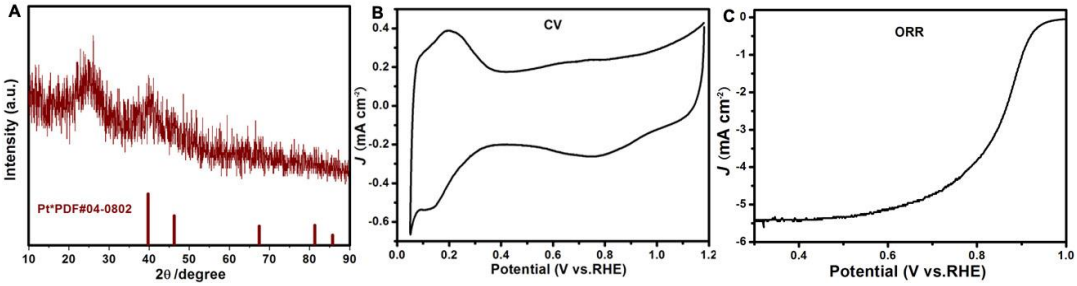

Figure S15. Characterization of Pt/CN$_x$/Co, related to Figure 5. (A) XRD patterns for Pt/CN$_x$/Co. (B) CV and (C) ORR curves of Pt/CN$_x$/Co catalyst.

Table S1. The element content and geometric analysis for the series of Pt/CN$_x$/TM samples, related to Figure 5.

	Pt/CN$_x$	Pt/CN$_x$/Ni	Pt/CN$_x$/Co	Pt/C (Alfa)
Element content Determined by XRF (wt.%)	Pt: 6.0%	Pt: 6.2%, Ni: 5.6%	Pt: 6.5%, Co: 4.8%	Pt: 20%
Specific ECSA (m^2/g_{Pt})	Initial: 125.5 CV-10 k: 115.6 CV-30 k: 94.2 CV-50 k: 91.5	Initial: 122.0 CV-10 k: 125.9 CV-30 k: 110.2 CV-50 k: 109.4	Initial: 121.6	Initial: 77.2 CV-10 k: 64.2 CV-30 k: 50.3 CV-50 k: 46.4

Transparent Methods

Materials Synthesis

Nano carbon support (Vulcan XC-72R). A desired amount of commercial Vulcan XC-72R was dispersed in acetone, stirred for 3 h at room temperature, filtered and dried in a vacuum oven at 343 K for 4 hours. Then, dispersing the resulted carbon powder in an aqueous solution of 10% nitric acid and 30% hydrogen peroxide (V_{HNO3} : V_{H2O2} = 2:1) and stirring at 333 K for 5 hours with reflux. The carbon support was obtained after suction filtering, water washing to neutral, drying in a vacuum oven at 353 K.

Preparation of NiO/C. The NiO/C powder was prepared by an incipient-wetness impregnation method. Briefly, 200 mg carbon support was mixed with moderate amounts of nickel nitrate solution with desired concentration, stirred and agitated by ultrasonic for 20 min. The obtained powder was dried at 353 K overnight and calcined at 573 K for 1 h in argon.

Preparation of CN_x/Ni support. The composite with Ni NPs capped by CN_x layer (CN_x/Ni) was prepared by encapsulating polymer of ethylenediamine and carbon tetrachloride on NiO/C and carbonizing in inert atmosphere according to our previous work (Fu et al., 2014). Specifically, 100 mg NiO/C powder was dispersed in 15 mL *m*-xylene by ultrasonic. 250 mg ethylenediamine and 500 mg carbon tetrachloride were dropwise added into the above suspension sequentially. Then, the suspension was stayed at 363 K for 4 h and 413 K for another 4 h, respectively. After cooling to room temperature, the polymer-coated NiO/C powder was washed with *m*-xylene and dried at 393 K overnight. The CN_x/Ni/C support, abbreviated as CN_x/Ni in the context, was obtained after carbonizing at 873 K for 6 h and 1173 K for 30 min in flowing N_2. The NiO was reduced to metallic Ni in the reducing atmosphere during the treatment at high temperatures.

Preparation of Pt/CN_x/Ni catalyst. In order to avoid the formation of Ni-Pt alloy, the CN_x/Ni support was refluxing in 1 M H_2SO_4 at 353 K for 4 h before loading Pt NPs. Because of the high graphitization, the CN_x shell is hydrophobic and cannot offer sites to anchor metal nanoparticles. To solve the problem, the CN_x shell was coated by a little amount of polydopamine with the following steps. 50 mg of CN_x/Ni powder was dispersed in 1mg/mL dopamine solution, which was prepared by dissolving dopamine hydrochloride in 10 mM tris buffer solution (pH 8.5). After stirring in air for 30 min, the surface-modified CN_x/Ni support was obtained by centrifugation and dehydration. The deposition of Pt NPs on CN_x/Ni support was operated by an incipient-wetness impregnation method. That is, transferring the as-obtained surface-modified CN_x/Ni into moderate amounts of chloroplatinic acid solution with desired concentration, dispersing and agitating by ultrasonic for 40 min and staying at room temperature overnight. After drying at 343 K, the chloroplatinic acid was reduced at 673 K for 3 h in 5.05 vol.% H_2/N_2 mixed gas with a heating rate of 2 °C/min.

Preparation of Pt/CN_x/Co catalyst. The Pt/CN_x/Co catalyst was prepared using a same procedure with Pt/CN_x/Ni, just substituting the nickel nitrate solution with cobalt nitrate solution in the preparation of CoO/C.

Characterization. X-ray diffraction (XRD) patterns were collected on a Phillips X'pert Pro diffractometer with Co Kα radiation at 40 kV and 35 mA. Field Emission High Resolution TEM and Energy-dispersive X-ray spectroscopy (EDX) were collected on Tecnai G2 F30 S-Twin TEM with an accelerating voltage of 300 kV. The X-ray photoelectron spectroscopy (XPS) tests were performed on a PHI 5000 Versa Probe equipped with a hemispherical electron analyzer and monochromatic Al Kα X-ray exciting source. Thermogravimetric (TG)

curves were collected on a STA 449C-Thermal Star 300 instrument (Netzsch, Germany) in air atmosphere with a heating rate of 10 $K \cdot min^{-1}$ to 1073 K. Redox of O_2-H_2 titration profiles were recorded on a thermal conductivity detector with the following procedure. 0.1 g sample was pretreated in 5.05 vol. % H_2/N_2 flow at 300 °C for 1 h and cooled to 30°C and then switched to oxygen. After putting the sample in O_2 flow at 30 °C for 1 h, switching O_2 to 5.05 vol. % H_2/N_2 flow to purge the adsorbed O_2 physically. Finally, raising the temperature from 30 to 700 °C at a rate of 10 °C min^{-1} under 5.05 vol. % H_2/N_2 flow and measuring the reduction curve.
s (229.2 m^2/g) and *n* are the surface area of C and the number of Ni nanoparticles on 1g C.

The number of layers (*n*) of wrapped CN_X:

$$n = \frac{m}{\rho \cdot s \cdot d} \quad \text{(S1)}$$

m and ρ (2.25 g/cm^3) (Ci et al., 2007) are the quality and density of CN_X, *s* (116.3 m^2/g) is the superficial area of NiO/C, *d* (0.32-0.5 nm) (Lee et al., 2008; Zhao et al., 2014; Jiang et al., 2016) is the thickness of monolayer CN_X.

The distance of adjacent Ni nanoparticles:

$$d_{Ni} = 2(s/n\pi)^{1/2} \quad \text{(S2)}$$

The specific surface area of the Pt NPs:

$$s = 4\pi r^2 * 1 / (\rho * 4/3\pi r^3) \quad \text{(S3)}$$

ρ (21.45 g/cm^3) is the density of Pt.

Electrochemical experiment. The electrochemical tests were performed on an electrochemical workstation (CHI 730D) using a three-electrode system. The catalyst ink was prepared by dispersing the obtained powder (5 mg) in isopropanol (970 μL) and 5 wt. % Nafion (30 μL) mixed solution by ultrasonic dispersion. Subsequently, 5 μL of the ink was transferred onto a glassy carbon electrode (φ = 5.6 mm, 0.246 cm^{-2}) and dried at room temperature. Pt wire and Ag/AgCl electrode were used as the counter and reference electrodes in 0.1 M $HClO_4$ solution, respectively.

Cyclic voltammetry (CV) was conducted at the potential of 0.05-1.2 V (*vs*. RHE) with a scan rate of 5 mV s^{-1} in N_2-saturated electrolyte.

CO-stripping voltammetry was conducted at the potential of 0.06-1.0 V (*vs*. RHE) with a scan rate of 50 mV s^{-1}. Prior to this, the working electrode was inserted into N_2-saturated electrolyte and held at the potential of 0.06 V (*vs*. RHE) for 15 min to electrochemically clean the catalyst surface. Then, CO was bubbled into the electrolyte while holding the potential at 0.06 V (vs. RHE) to poison the electrode surface. Afterwards, N_2 was bubbled into the electrolyte to remove the residual CO.

RDE system was used to study the ORR activity in O_2-saturated electrolyte at the potential of 0.05-1.2 V (*vs.* RHE) with a scan rate of 20 mV s^{-1} and rotation rate of 1600 rpm at 298 K. All the ORR curves were iR corrected. The accelerated deterioration tests (ADTs) was completed by applying the cyclic voltammetry between 0.6 and 1.0 V (*vs.* RHE) with a sweep rate of 200 mV/s for 50,000 cycles in O_2-saturated electrolyte.

The conduction band (CB) level of the samples were determined from the linear potential plots based on the Mott-Schottky equation. The linear potential plots were measured by electrochemical impedance spectroscopy (EIS) using a conventional three-electrode system, in which the Pt wire and Ag/AgCl electrode were used as the counter and reference electrode, respectively. The working electrode was prepared by dripping catalyst ink on a glassy carbon electrode (φ = 0.5 mm) and drying at room temperature. The measurements were performed in darkness at a scan rate of 25 mV/s and a frequency of 1 kHz.

Supplementary References

Ci, L., Vajtai, R. and Ajayan, P. M. (2007) Vertically aligned large-diameter double-walled carbon nanotube arrays having ultralow density. J. Phys. Chem. C *111*, 9077-9080.

Fu, T., Wang, M., Cai, W., Cui, Y., Gao, F., Peng, L., Chen, W., and Ding, W. (2014). Acid-resistant catalysis without use of noble metals: carbon nitride with underlying nickel. ACS Catal. *4*, 2536-2543.

Jiang, W., Luo, W., Zong, R., Yao, W., Li, Z., and Zhu, Y. (2016) Polyaniline/Carbon Nitride Nanosheets Composite Hydrogel: A Separation-Free and High-Efficient Photocatalyst with 3D Hierarchical Structure. Small *12*, 4370-4378.

Lee, C., Wei, X., Kysar, J. W. and Hone, J. (2008) Measurement of the elastic properties and intrinsic strength of monolayer graphene. Science *321*, 385-388.

Stephens, I., Bondarenko, A., Grønbjerg, U., Rossmeisl, J. and Chorkendorff, I. (2012). Understanding the electrocatalysis of oxygen reduction on platinum and its alloys. Energy Environ. Sci. *5*, 6744-6762.

Zhao, Y., Li, X., Du, Y., Chen, G., Qu, Y., Jiang, J., and Zhu, Y. (2014) Strong light-matter interactions in sub-nanometer gaps defined by monolayer graphene: toward highly sensitive SERS substrates. Nanoscale *6*, 11112-11120.